Capturing the signature of heavy rainfall events using the 2-d-/4-d water vapour information derived from GNSS measurement in Hong Kong

Qingzhi Zhao [1,*], Yibin Yao [2], Wanqiang Yao [1] and Kefei Zhang[3]

[1] College of Geomatics, Xi'an University of Science and Technology, Xi'an 710054, China; zhaoqingzhia@163.com; sxywq@163.com

[2] School of Geodesy and Geomatics, Wuhan University, Wuhan 430079, China; ybyao@whu.edu.cn

[3] School of Environment Science and Spatial Informatics, China University of Mining and Technology, Xuzhou, China; kefei.zhang@rmit.edu.au

* Correspondence: zhaoqingzhia@163.com; Tel.: +86-182-9185-5186

Abstract: Apart from the well-known applications like positioning, navigation and timing (PNT), Global Navigation Satellite System (GNSS) has manifested its ability in many other areas that are vital to society largely. With the dense setting of the regional continuously operating reference station (CORS) networks, monitoring the variations in atmospheric water vapour using a GNSS technique has become the focus in the field of GNSS meteorology. Most previous studies mainly concentrate on the analysis of relationship between the two-dimensional (2-d) Precipitable Water Vapour (PWV) and rainfall while the four-dimensional (4-d) variations of atmospheric water vapour derived from the GNSS tomographic technique during rainfall events are rarely discussed. This becomes the focus of this work, which investigates the emerging field of GNSS technology for monitoring changes in atmospheric water vapour during rainfall, especially in the zenith direction. This paper includes an analysis of both 2-d PWV and 4-d atmospheric water vapour profiles. A period with heavy rainfall events in this study was selected to capture the signature of atmospheric water vapour variation using the ground-based GNSS tomographic technique. GNSS observations from the CORS network of Hong Kong were used. Analysed results of the 2-d PWV/4-d water vapour profiles change during the arrival, occurrence and depression of heavy rainfall show that: (i) the PWV time series shows an increasing trend before the arrival of heavy rainfall and decreases to its average value after the depression of rainfall; (ii) rainfall leads to an anomalous variation in relative humidity and temperature while their trends are totally opposite and show daily periodicity for periods without rain (this is highly correlated with the changes in

solar radiation); (iii) atmospheric water vapour presents unstable conditions with intense vertical convective motion and hydrometeors are formed before the arrival of rainfall while returning to relatively stable conditions during heavy rainfall. This study indicates the potential for using GNSS-derived 2-d PWV and 4-d water vapor profiles to monitor spatio-temporal variations in atmospheric water vapour during rainfall, which provides a better understanding of the mechanism of convection and rainfall induced by the extreme weather events.

Keywords: GNSS; PWV; water vapor profiles; extreme weather events

1 Introduction

Precipitable water vapour (PWV), which refers to the total content of integrated water vapour density along the zenith direction, is a significant component reflecting the short-term atmospheric water vapour variations used in severe weather detection (Shoji, 2009, 2013; Bai, 2004) as well as in long-term climate studies (Gradinarsky et al., 2002, Vey et al., 2010; Ning et al., 2012; Liu et al., 2013; Bock et al., 2014). However, it is difficult to obtain a satisfactory spatio-temporal resolution of atmospheric water vapour due to the limitation of both the number of radiosondes and the observation times (Brenot et al., 2013; Zhang et al., 2015). For the past 20 years, the ability to estimate water vapour content with an accuracy of 1 to 2 mm has been proved using the Global Navigation Satellite System (GNSS) technique, which generally formed a new field of study in GNSS Meteorology (Bevis et al., 1992). Therefore, the variation of atmospheric water vapour with high accuracy, as well as the high spatio-temporal resolution can be obtained using the hyper-dense GNSS networks (with receivers only a few kilometres apart).

GNSS PWV can be used to provide information about water vapour distribution, which is related to form of precipitation and not only to severe weather events. (Zhang et al., 2015; Yao et al., 2017; Zhao et al., 2018a, 2018b). GNSS PWV is operationally used for their assimilation into numerical weather prediction models (NWM) than just for operational meteorology (JMA, 2013; Bennitt and Jupp, 2012; Guerova et al., 2016; Barindelli et al., 2018). In those areas, the zenith total delays (ZTD) or PWV estimated from ground-based GNSS measurements are generally assimilated into numerical weather prediction (NWP) models (De Haan 2013; Saito et al., 2017). In addition, ZTD or PWV can be used for early warnings than that it is used, which has been investigated in areas of Greater Lisbon in Portugal as well as Zhejiang Province in China (Brenot et al., 2013; Benevides

et al., 2015; Yao et al., 2018; Zhao et al., 2018a, 2018b). These applications have verified the ability of GNSS as used in meteorology, but those cases are mainly focussed on two-dimensional (2-d) PWV which cannot reflect the specific vertical variations in atmospheric water vapour.

Although GNSS tropospheric tomography has been proposed (Flores et al., 2000), and can be used to obtain four-dimensional (4-d) water vapour variations, the development of this technique has mainly focussed on the improvement of theoretical and model aspects while its application is rarely discussed. For example, the reliability of GNSS tomography was validated using radiosonde data by Troller et al. (2006) and Shangguan et al. (2013). The joint reconstruction of atmospheric water vapour was also investigated by combing multi-GNSS observations as well as multi-source data derived from the GNSS Radio occultation technique, Interferometric Synthetic Aperture Radar (InSAR), radiosonde, *etc*. (Bender and Raabe, 2007; Bender et al., 2011; Wang et al., 2014; Alshawaf, 2013; Heublein et al., 2015; Benevides et al., 2015; Zhao et al., 2018c). For the improvement of tomographic models and resolution thereof, Perler et al. (2011) proposed a new parameterised tomographic method, which is capable of obtaining better tomographic results. Some methods concerned with the resolution of tomographic models have been proposed such as the extended sequential successive filtering method. (Braun et al, 2003, 2004; Wang et al., 2014; Zhao et al., 2017a, 2018d; Chen and Liu, 2014). In addition, maximal use of GNSS signals penetrating from the side faces of tomography areas has obtained a significant improvement and is realised by introducing the water vapour scale factor (Yao and Zhao, 2016; Yao et al., 2016; Zhao et al., 2017b).

Currently, GNSS tomography technique is maturing in terms of theoretical and model aspects through almost 20 years of development, but its application in GNSS meteorology remains to be further investigated, therefore, we focus on capturing the signature of heavy rainfall events using the 2-d/4-d water vapour information derived from GNSS measurements in Hong Kong. The 2-d PWV time series is first analysed for correlation with heavy rainfall. Thereafter, the signatures of 4-d water vapour variations derived from GNSS tomography are investigated during heavy rainfall events while the tomographic modelling is resolved using the optimal weighting determination method.

2 Fundamentals of GNSS meteorology

2.1 Retrieval of GNSS PWV

Satellite signals are delayed and bent when crossing the troposphere, which can be divided into two parts: hydrostatic delay and non-hydrostatic delay. The first part in a zenith direction, also called zenith hydrostatic delay (ZHD), can be precisely calculated by the Saastamoinen model (Saastamoinen, 1972) with the observed surface pressure. The second part can be estimated in the zenith direction using GNSS data, which is also called zenith wet delay (ZWD), from which the PWV can be calculated. Therefore, GNSS meteorology is formed, as first proposed by Bevis et al. (1992). The calculation used in obtaining PWV is expressed as follows: the zenith total delay is first estimated by processing the GNSS observations using the GNSS processing software such as Bernese (Dach et al., 2015), GAMIT (Herring et al., 2010), *etc*. In the GNSS data processing, the ZHD is usually taken from an a priori model and later precisely computed from i.e. real meteorological observation. The ZWD is then obtained by extracting the ZHD from ZTD and thus the PWV can be calculated based on the following equations (Saastamoinen, 1972; Askne and Nordius, 1987; Bevis et al., 1992):

$$\begin{aligned} &\mathrm{PWV}=\Pi\cdot\mathrm{ZWD}\\ &\Pi=10^{6}\Big/\left(\left(k_{2}^{'}+k_{3}/\mathrm{Tm}\right)\cdot R_{v}\cdot\rho_{w}\right)\\ &\mathrm{ZWD}=\mathrm{ZTD}\text{-}\mathrm{ZHD}\\ &\mathrm{ZHD}=\frac{0.002277\times\mathrm{P}}{1-0.00266\times\cos(2\varphi)-0.00028\times\mathrm{H}} \end{aligned} \tag{1}$$

Where Π refers to the conversion factor. $k_2^{'}$, k_3, and R_v are constants with values of 22.1 K/hPa, 3.739 × 10^5 K^2/hPa and 461.495 J/kg/K, respectively. T_m represents the weighted mean temperature, which is related to surface parameters such as temperature and pressure. Therefore, T_m is usually calculated based on the empirical model using the data from radiosonde or numerical weather model due to the observed layered meteorological parameters which are rarely obtained (Bevis et al., 1994; Yao et al., 2012). In the fourth formula in Eq. (1), P, H and φ represent the surface pressure (hPa), geodetic height (km) and station latitude (rad), respectively. In our study, the value of T_m is calculated based on the established regional T_m model using the radiosonde data and observed temperature (Section 3.2).

2.2 Establishment of tomographic model

Generally, the slant wet delay (SWD) or slant integrated water vapour (SIWV) is considered as the input information for GNSS troposphere tomography (Flores et al., 2000; Hirahara, 2000; Skone and Hoyle, 2005; Rohm and Bosy, 2009; Chen and Liu., 2014) and the following equation gives an expression used to obtain SIWV (Flores et al., 2000):

$$\mathrm{SIWV}_{azi,ele} = m_w(ele)\cdot \mathrm{PWV} + m_w(ele)\cdot cot(ele)\cdot (G_{NS}^w \cdot cos(azi) + G_{WE}^w \cdot sin(azi)) \quad (2)$$

Where m_w represents the gradient mapping function, and global mapping function (GMF) is used in our experiment (Böhm et al., 2006). ele and azi refer to the elevation angle and azimuth angle, respectively. G_{NS}^w and G_{WE}^w are the horizontal tropospheric gradient parameters of ZWD in the south-north and west-east directions, respectively, which are caused by the atmospheric inhomogeneous. Additionally, a post-fit residual for SIWV is existed, which contains some information about tropospheric water vapor distribution during the severe weather events and cannot captured by ZTD or gradients (Kacmarík et al., 2017).

If a sufficient number of SIWVs derived from some stations in a regional CORS network can be obtained, the GNSS tomographic technique can be used to reconstruct the three-dimensional (3-d) distribution of atmospheric water vapour field. Therefore, a four-dimensional (4-d) water vapour information is a time series of such a 3-d tomographic result, which can be used to reflect the regional atmospheric water vapour variations in both the spatial and temporal domains. As described by Flores et al. (2000), the linear observation equation between SIWV and water vapour density can be expressed as follows:

$$\mathrm{SIWV} = \sum (d_{ijk} \cdot x_{ijk}) \quad (3)$$

Where i, j and k represent the location of the area of interest in the longitudinal, latitudinal, and zenith directions, respectively. d_{ijk} and x_{ijk} refer to the distance travelled by satellite signals and the water vapour density remains to be estimated, respectively in the discretized voxels (i, j, k). Therefore, the matrix form of the tomographic observation equation can be described as follows:

$$\mathbf{y} = \mathbf{A}\cdot\mathbf{x} \quad (4)$$

Where $\mathbf{y}$ represents the column vector of SIWV derived from GNSS measurements. $\mathbf{A}$ and $\mathbf{x}$ are the coefficient matrix of distance penetrated by satellite rays and the column vector of

146 water vapour density, respectively.

147 Although Rohm (2013) developed a GNSS tomography solution using no constraints, most studies
148 still used some constraints to overcome the influence caused by the ill-posed problem in the
149 inversion of the tomographic normal equation (Flores et al., 2000; Bi et al., 2006; Bender et al.,
150 2011; Rohm and Bosy, 2011 Chen and Liu, 2014). In our study, both horizontal and vertical
151 constraints are considered. The water vapour density in a certain voxel is regarded as the weighted
152 mean value of its horizontal neighbouring voxels (Rius et al., 1997) and the negative exponential
153 function is introduced to describe the relationship between the nearby voxels in the zenith
154 direction while the coefficients of functional model are established using radiosonde data (Yao and
155 Zhao, 2016). Consequently, the tomographic modelling can be expressed after imposing the
156 constraints as:

157
$$\begin{pmatrix} \mathbf{y} \\ \mathbf{0} \\ \mathbf{0} \end{pmatrix} = \begin{pmatrix} \mathbf{A} \\ \mathbf{H} \\ \mathbf{V} \end{pmatrix} \cdot \mathbf{x} \tag{5}$$

158 Where $\mathbf{H}$ and $\mathbf{V}$ are the coefficient matrices of horizontal and vertical equations, respectively.
159 To obtain a reasonable tomographic result from the above equation, an optimal tropospheric
160 solution method is used, which can adaptively tune the weightings of different types of equations
161 (Zhao et al., 2018d).

162

163 ## 3 Data description and establishment of a regional T_m model

164 ### 3.1 Data description

165 To validate the ability of GNSS technique in capturing the signature of atmospheric water vapour
166 variation during heavy rainfall events, two periods of GNSS observations (19 to 27, July 2015 and
167 1 to 8, August 2015) from 13 GNSS stations in the CORS network of Hong Kong are selected in
168 the experiment. Those two periods are selected because they correspond to a heavy rainfall event
169 and a no-rainfall event, respectively according to hourly rainfall data from 45 rain gauges evenly
170 distributed across this area (Figure 1). There is a radiosonde station located in this area where the
171 radiosonde balloon is launched twice daily at UTC 00:00 and 12:00, respectively. The 20-years of
172 radiosonde data from 1998 to 2017 are used to establish the regional T_m model in this study. In
173 addition, the surface temperature and relative humidity are also selected to analyse their changes

during those two periods. To explain the variations of surface temperature and relative humidity, the solar radiation data are also used in this study, which is derived from the CRU-NCEP Ver. 7 dataset (Wu et al., 2015). This dataset is a combination product of the CRU TS3.2 climate dataset and the NCEP reanalysis data. The temporal-spatial resolution of the solar radiation dataset are four times daily (UTC 00:00, 06:00, 12:00 and 18:00) and 0.5°×0.5°, respectively.

GNSS observations are processed using Precise Point Positioning (PPP) data processing software developed by our research group. The post-processing mode is used and the orbit and satellite clock errors are corrected using the final products downloaded from ftp://ftp.gfz-potsdam.de/. The GMF is selected (Böhm et al., 2006) while the cut-off elevation angle is 7° in our experiment. The sampling rate of GPS observation is 30s and the and the ZTD parameter is estimated every 5 minutes. The gradient parameters in south-north and east-west directions are also estimated at intervals of 2 h. The detailed description of processing strategy has been presented in Zhao et al. (2018d). The root-mean-square error (RMSE) of the estimated ZTD parameter has been proved with the values of 7.2 mm and 8.1 mm when the ZTD estimated from the GAMIT (v10.5) and Bernese (v5.2) software based on the double-difference model are regarded as references, respectively (Zhao et al., 2018a). Due to the accurately ZHD parameter can be estimated using the empirical model, therefore, the final error in the estimated PWV values is approximately 1-1.5mm (Zhao et al., 2018e). The corresponding meteorological parameters, such as the surface pressure and temperature, are also obtained at the selected GNSS stations. Therefore, the precise ZHD can be calculated by the empirical model using the observed surface pressure. The conversion factor, as described in Eq. (1), is also obtained, in which T_m is calculated based on the established T_m model which will be introduced in the following section. Finally, the PWV time series, as well as the SIWVs for the 13 selected GNSS stations, can be obtained. Five of the 45 rain gauges (R21, TMS, PEN, SSP, and KSC) are selected to analyse the variations in atmospheric water vapour during different weather conditions (Figure 1).

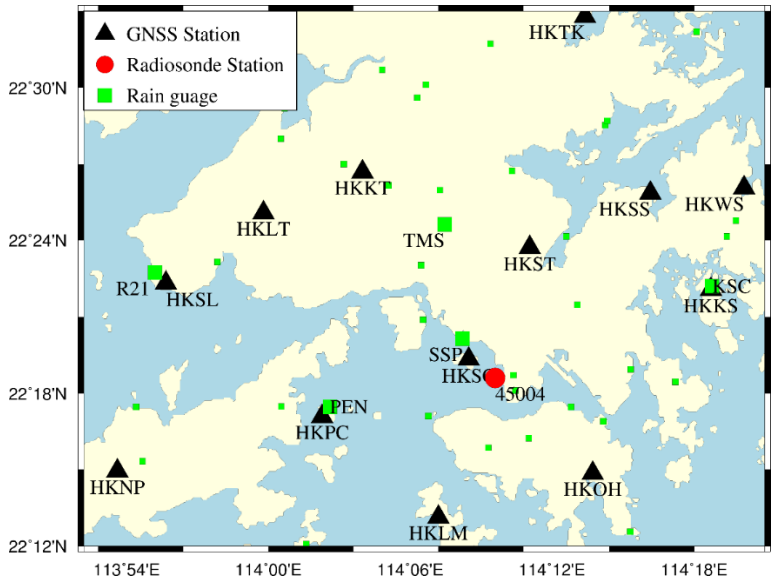

Figure 1. Geographic distribution of selected GNSS and radiosonde stations as well as the rain gauges used in the experiment

3.2 Establishment of the regional T_m model

Due to the layered information about vertical profile of some meteorological parameters as water vapour pressure or air temperature is generally unavailable for the location of GNSS stations, therefore, the T_m values of those stations are calculated based on the empirical model in this experiment. It has been proved that T_m is highly correlated with the variations of temperature, pressure, and the seasons (Bevis et al., 1992; Yao et al., 2012; Yao et al., 2014, 2015; Liu et al., 2018). Therefore, a regional T_m model which includes as parameters: temperature, surface pressure, and seasonal variation, is established and expressed as follows:

$$T_m = T_{m0} + a*T_s + b*P_s + c*\cos(2\pi\frac{doy}{365.25}) + d*\sin(2\pi\frac{doy}{365.25}) + e*\cos(4\pi\frac{doy}{365.25}) + f*\sin(4\pi\frac{doy}{365.25}) \quad (6)$$

Where T_{m0}, T_s and P_s represent the initial value of T_m, surface temperature and surface pressure, respectively; doy refers to the day of year; a and b are coefficients of T_s and P_s, respectively, while c to f refer to the coefficients of the seasonal correction function. In our study, the coefficients in Eq. (6) were obtained by the least square regression method using 20-year radiosonde data for 45004 while the values of a to f are 129.1225, 0.5370, -0.0023, 0.358, 0.813, -0.178, and 0.255, respectively.

The performance of the established T_m model is analysed and compared with the empirical formula proposed by Bevis et al. (1994). Statistical result of 20-years of radiosonde data reveals that when compared to the T_m values calculated using the observed radiosonde data, the standard deviation and bias for the established T_m model and the empirical formula proposed by Bevis et al. (1994) are 2.04/0.0009 K and 3.41/2.53 K, respectively, which indicates that the established regional T_m model shows a good result in research area. To further analyse the impact of T_m model error on the calculated PWV, a comparison experiment is carried out for radiosonde station 45004 with a variation in T_m of 1 K, 3 K, 5 K, 7 K, and 9 K, respectively and compared with the actual PWV values over the period of 1998 to 2017. Statistical analysis shows that the PWV errors induced by the change in T_m of 1 K, 3 K, 5 K, 7 K, and 9 K are 0.15 mm, 0.45 mm, 0.75 mm, 1.04 mm, and 1.34 mm, respectively under the condition of PWV > 0 mm, while the values are 0.18 mm, 0.54 mm, 0.91 mm, 1.27 mm, and 1.63 mm, respectively when PWV > 40 mm. Therefore, the PWV errors caused by the established T_m model in this study are less than 0.4 mm and 0.5 mm when PWV > 0 mm and PWV > 40 mm, respectively. Such result is deemed acceptable for the analysis of PWV variations with rainfall events (Akilan et al., 2015) and corresponds to the previous result obtained from Guerova et al. (2016).

4 Signature of 2-d/4-d variations in atmospheric water vapour during rainfall

According to the recordings derived from the Hong Kong Observatory, the convectional rain happened during the period of 19 to 27, July 2015. It is continuous rains in Hong Kong and the hourly rainfall have been accumulated for 45 rain gauges with the largest rainfall more than 300 mm for the entire experimental period in HKSC station. The weather conditions are cloudy and sunny without rainfall happened for the period of 1 to 8, August 2015. Therefore, those two periods are selected in this paper to investigate the variation characteristics of atmospheric water vapor.

4.1 Cases of 2-d PWV time series change

To capture the signature of PWV time series change in different weather conditions, the comparison between the 5-minute GNSS-derived PWV and hourly rainfall are performed for the periods of 19 to 27, July 2015 and 1 to 8, August 2015, respectively. Four GNSS stations (HKKS, HKSC, HKPC, and HKSL) and the surrounding rainfall gauges (HSC, SSP, PEN, and R21) are

selected for this experiment. Additionally, other meteorological parameters (temperature, relative humidity and solar radiation) are also analysed during this experimental period.

Figure 2 shows the variations of 5-minute PWV time series data with hourly rainfall as well as the cumulative rainfall at those four stations for the period of 19 to 27, July 2015. It can be seen from the first column of Figure 2 that the PWV time series show an increasing trend before the arrival of rainfall and reaches a relatively large value during rainfall, PWV then returns to its average value after rainfall. Such phenomenon found above can be used to forecast the nowcasting rainfall (Yao et al., 2017; Zhao et al., 2018a). The second column of Figure 2 reveal that the cumulative rainfall first increased at about UTC 11:00, 20 July, 2015 with different levels reached and the event terminated at UTC 12:00, 23 July, 2015. The largest cumulative rainfall reached more than 300 mm at HKSC station while the minimum recorded rainfall was about 100 mm at HKSL station across the four selected gauge stations. The PWV time series is also analysed at those four stations for the period from 1 to 8, August, 2015 in which no rainfall was recorded (Figure 3). Figure 3 shows the 5-minute PWV time series changes from which it can be found that PWV does not show any continuous increasing trend when there is no rainfall, but the range of PWV variation is relatively large (from about 35 mm to greater than 55 mm). Comparing the PWV time series in Figures 3 and 4, it also can be observed that the PWV values during rainfall are much larger than that of no rainfall time at the situation occurred in the selected time periods.

In addition, 5-minute surface temperature and relative humidity data are also analysed during those two periods. The first and second columns of Figure 4 show the changes in temperature and relative humidity for the period 19 to 27, July, 2015. It also can be seen that the temperature and relative humidity do not show any trend during heavy rainfall but show a tendency to run counter to one another on 19, 26, and 27, July. one explanation is that heavy rainfall breaks the trend in temperature and relative humidity for the period from 20 to 25, July, 2015. The third column of Figure 4 shows the changes in solar radiation for this period, from which it can be observed that the solar radiation undergoes a day periodic change. To verify this explanation, the variations of temperature and relative humidity, as well as those in solar radiation, are also presented at those four stations for period of 1 to 8 August without rainfall (Figure 5): temperature and solar radiation show a similar trend while relative humidity presents the opposite trend. Additionally, it can be observed from the first and third columns of Figures 5 that the maximum values of solar

radiation and temperature occurred at UTC 4:00 (local time 12:00) while the minimum value of relative humidity also occurred at that time. The phenomenon found in Figure 5 further confirmed the explanation presented above. In addition, the values of solar radiation are more fluctuated at the four stations during rainfall when compared to that without rain (Figures 4 and 5): a possible reason for this is that the part of solar radiation is decreased by cloud cover during heavy rain.

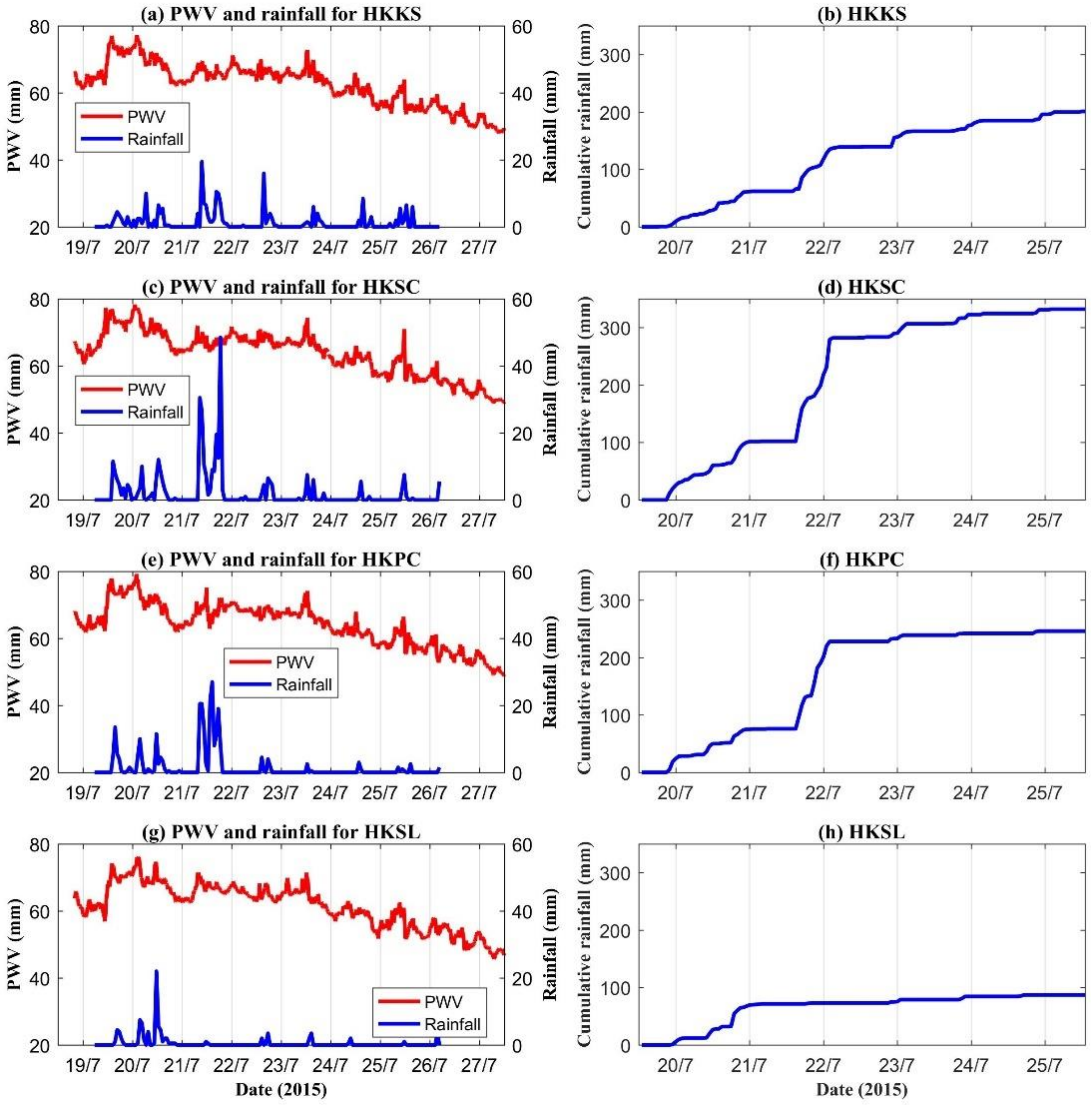

Figure 2. Variations of 5-minutely PWV time series with hourly rainfall and the cumulative rainfall for HKKS, HKSC, HKPC and HKSL stations over the period of 19 to 27, July 2015, the first column represents the variations of PWV and rainfall and the second column refers to the cumulative rainfall

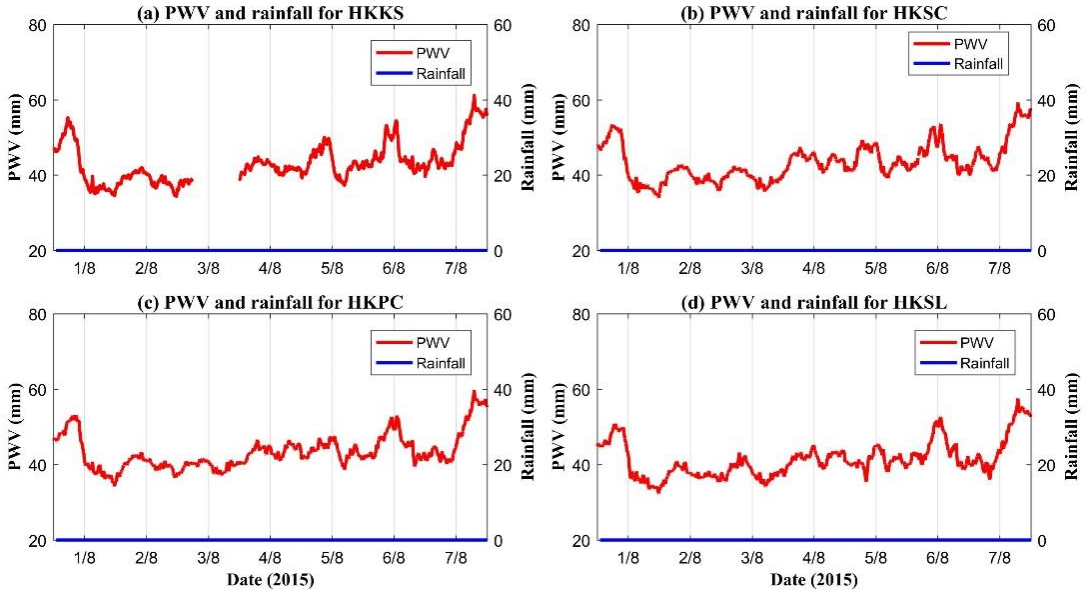

288

289 Figure 3. Variations of 5-minutely PWV time series with hourly rainfall at (a) HKKS, (b) HKSC,

290 (c) HKPC and (d) HKSL stations over the period of 1 to 7, August 2015

291

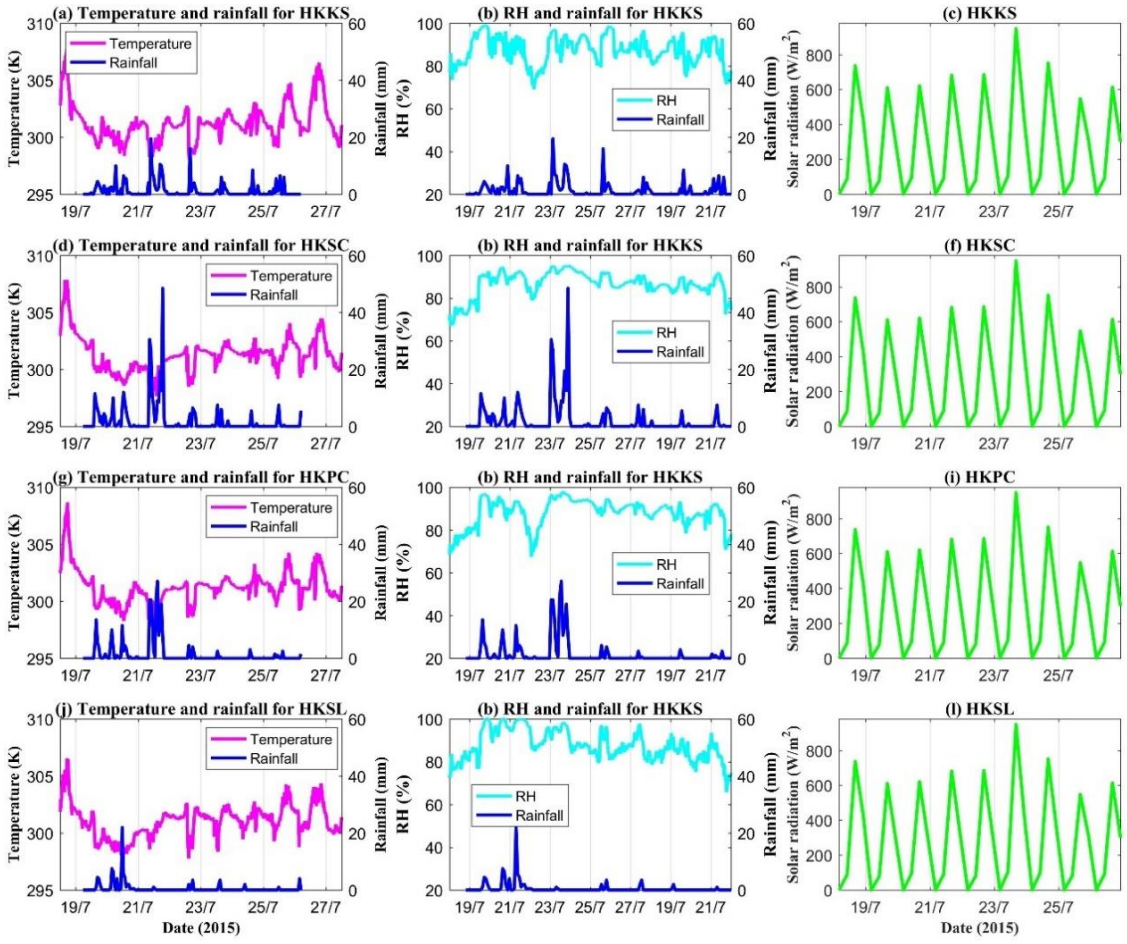

292

293 Figure 4. Changes of temperature, relative humidity with rainfall as well as the solar radiation at

HKKS, HKSC, HKPC and HKSL stations over the period of 19 to 27, July 2015, the first column represents the variations of temperature and rainfall, the second column refers to the variations of RH and rainfall and the third column refers to the solar radiation

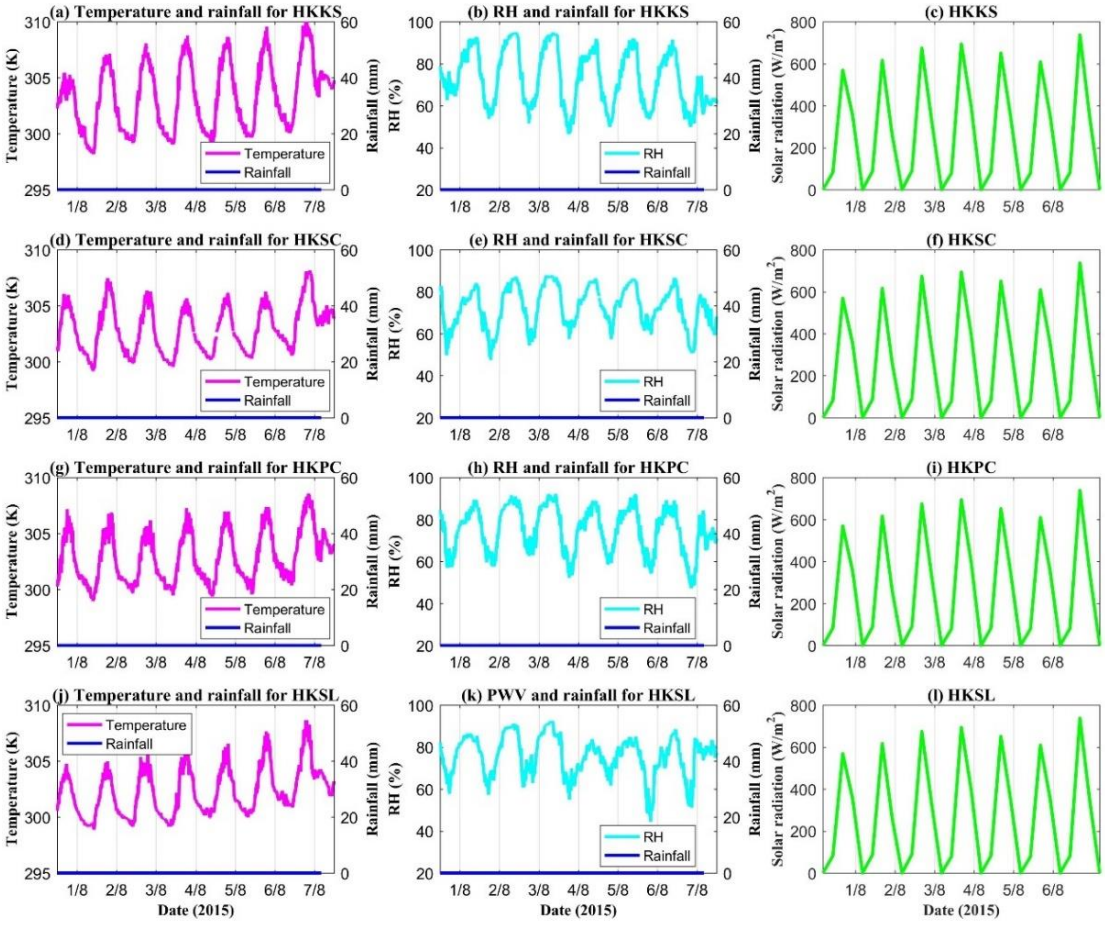

Figure 5. Changes of temperature, relative humidity with rainfall as well as the solar radiation at HKKS, HKSC, HKPC and HKSL stations over the period of 1 to 7, August 2015, the first column represents the variations of temperature and rainfall, the second column refers to the variations of RH and rainfall and the third column refers to the solar radiation

4.2 Cases of water vapour profile variation during heavy rainfall

The variations in 4-d atmospheric water vapour are also analysed during heavy rainfall. In this section, the tomographic technique is introduced and the research area is discretised. There are 7 and 8 grids in longitudinal and latitudinal directions, respectively and 29 layers in zenith direction. Therefore, there are total 7 × 8 × 29 voxels. The horizontal steps are 0.05° and 0.06° in

longitudinal and latitudinal directions, respectively while the inhomogeneous vertical step is selected based on the water vapour distribution at different altitudes (Yao and Zhao, 2017) with resolutions of 0.2 km × 10, 0.3 km × 8, 0.4 km × 6, 0.6 km × 4, and 0.8 km × 1, respectively. A comparison of water vapour density profiles derived from tomographic result and radiosonde data at the location of radiosonde station 45004 is first presented (Figure 6) to validate the performance of the GNSS tomographic technique. It can be seen from the Figure 6 that the profiles derived from tomographic results were consistent with the observed radiosonde data at most altitudes, which manifests the ability of the GNSS tomographic technique to reflect variations in water vapour content during rainfall. Due to this paper is mainly focus on the analysis of 4-d water vapour variation during the heavy rainfall events and the quality evaluations of vertical profiles from GNSS tomography reconstruction have been carried out by our research group for this research area in the previous studies (Yao and Zhao, 2016, 2017; Zhao et al., 2017a; Zhao et al., 2018d), therefore, more detailed comparison information is not presented.

Two heavy rainfall periods are selected in this experiment: the first at UTC 18 to 22, 21 July 2015 and three rain gauges are used to analyse the variations in water vapour profiles. The hourly rainfall for those three rain gauges is presented in Table 1 while the water vapour profile variations over time for SPP, PEN and TKL are shown in Figure 7. From this figure it can be observed that atmospheric water vapour profile undergoes vertical movement about 1-2 hours before the arrival of heavy rain, which is reflected by the fluctuating water vapour density at different altitudes. It can be observed from SPP rain gauge ((a1)-(h1)) that the water vapour content in the lower atmosphere increases from an altitude of about 1.8-2.5 km to 3.5 km while the water vapour content decreases from 4-5 km to 3.5 km. It can also be observed from PEN and TKL rain gauges ((a2)-(h2) and ((a3)-(h3))) that an upward and downward movement happened in the atmospheric water vapour profile in the lower and upper atmosphere, respectively: this results in a large increase in atmosphere water vapour at altitudes of about 2.3 km and 1.6 km, respectively (especially at PEN). The upward and downward motions of atmospheric water vapor in the lower and upper atmosphere are expected to the occurrence of the strong convective weather. The above phenomenon of vertical water vapor motion corresponds to the convectional rain reported. In addition, it was found that the variations of water vapour profiles in zenith direction at station TKL are weaker than that from stations PEN and SPP. A possible explanation is that the rainfall

was 30.5 mm and 20.5 mm for PEN and SPP at UTC 20, 21 July 2015 while the value is only 1 mm at station TKL at UTC 21, 21 July 2015 (Table 1). The above phenomenon indicates that the heavy rainfall could be induced by vertical motion of water vapour. The variations in water vapour profiles during rainfall reveal that the significant vertical motion of water vapour occurred before the onset of rainfall while the water vapour profiles were relatively stable during rainfall events. In addition, the time series of water vapour density profiles, at a temporal resolution of 1 minute, for the three rain gauges are also presented in Figure 8. From which it can be seen that the vertical water vapour density profile undergoes a significant vertical motion about 1-2 hours before the arrival of rain (black dotted rectangles, Figure 8) while the profiles are relatively stable during rain. By analysing the Figure 7, it also can be found that the vertical variations of water vapour density profiles at SPP and PEN stations 1 hour before rainfall are more active than that at TKL station: this can be explained by considering that the continued heavy rainfall happened at SPP and PEN stations while the TKL had little rainfall (Table 1), therefore, the continuing water vapour transportation in the zenith direction existed in the lower atmosphere at stations SPP and PEN.

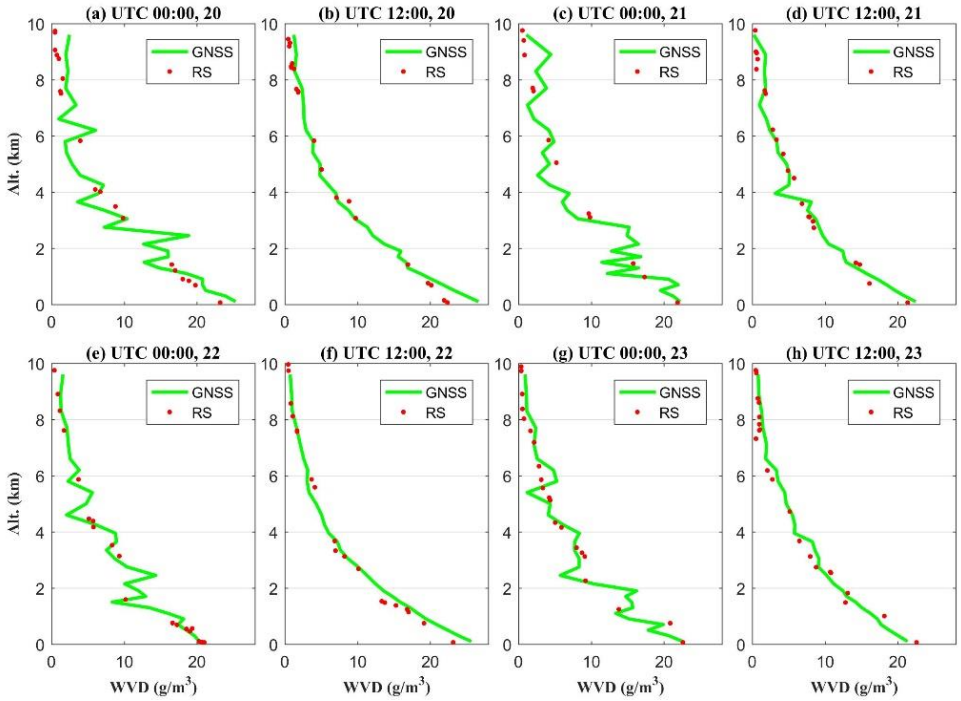

Figure 6. Distribution of water vapor density (WVD) profiles at UTC 00:00 and 12:00, respectively derived from the GNSS tomographic result (green curve) and the radiosonde data of the observed height (red hot) for the location of radiosonde station (45004) over the period of 20 to 23, July 2015

358 Table 1 Hourly Rainfall information of the selected four rain gauges over period of UTC 19 to 23,

359 21 July 2015 (Unit: mm)

Station / Date	SPP	PEN	TKL
19, 21 July	0	0	0
20, 21 July	30.5	20.5	0
21, 21 July	26.5	20.5	1.0
22, 21 July	10.5	13.5	1.5
23, 21 July	7.5	2.5	1.5

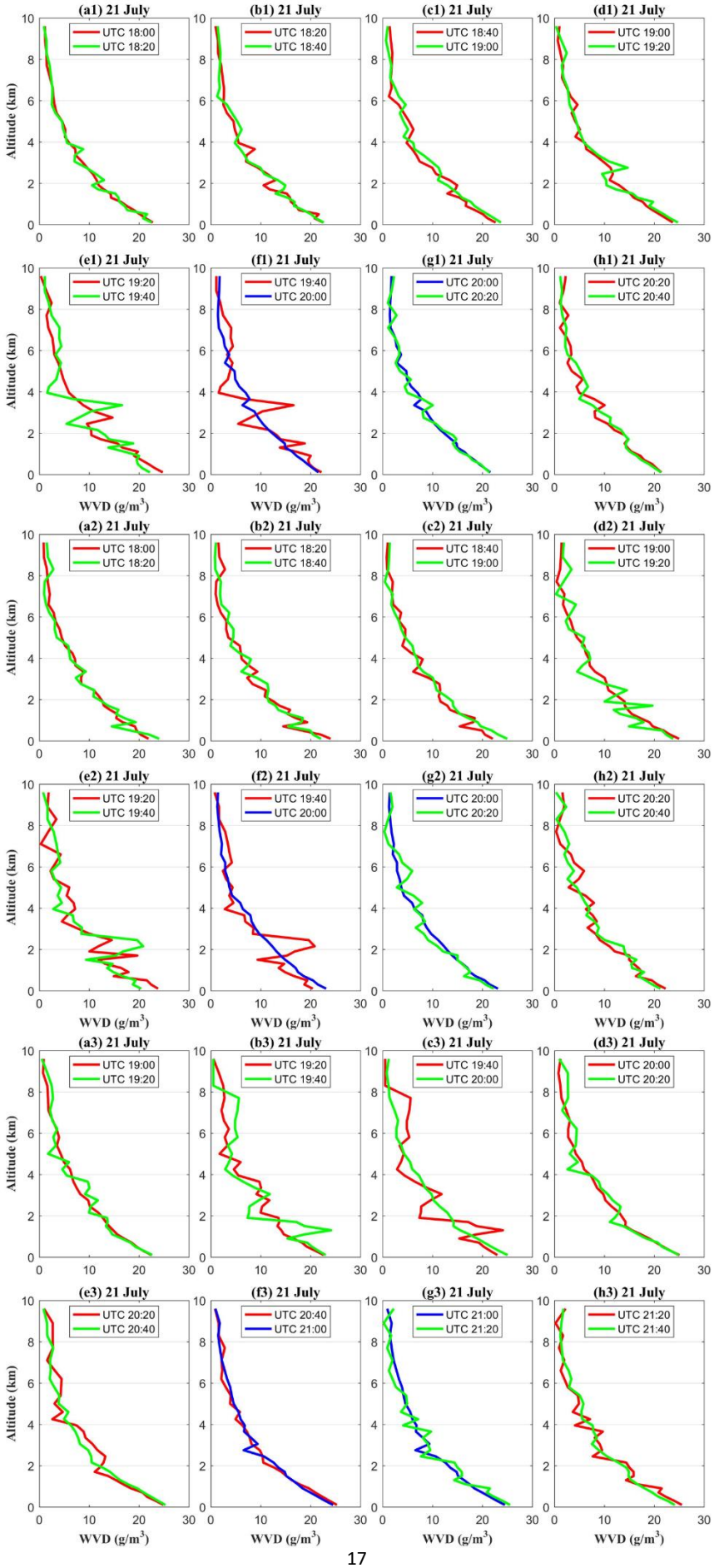
(a1) 21 July
UTC 18:00
UTC 18:20
(b1) 21 July
UTC 18:20
UTC 18:40
(c1) 21 July
UTC 18:40
UTC 19:00
(d1) 21 July
UTC 19:00
UTC 19:20
(e1) 21 July
UTC 19:20
UTC 19:40
(f1) 21 July
UTC 19:40
UTC 20:00
(g1) 21 July
UTC 20:00
UTC 20:20
(h1) 21 July
UTC 20:20
UTC 20:40
(a2) 21 July
UTC 18:00
UTC 18:20
(b2) 21 July
UTC 18:20
UTC 18:40
(c2) 21 July
UTC 18:40
UTC 19:00
(d2) 21 July
UTC 19:00
UTC 19:20
(e2) 21 July
UTC 19:20
UTC 19:40
(f2) 21 July
UTC 19:40
UTC 20:00
(g2) 21 July
UTC 20:00
UTC 20:20
(h2) 21 July
UTC 20:20
UTC 20:40
(a3) 21 July
UTC 19:00
UTC 19:20
(b3) 21 July
UTC 19:20
UTC 19:40
(c3) 21 July
UTC 19:40
UTC 20:00
(d3) 21 July
UTC 20:00
UTC 20:20
(e3) 21 July
UTC 20:20
UTC 20:40
(f3) 21 July
UTC 20:40
UTC 21:00
(g3) 21 July
UTC 21:00
UTC 21:20
(h3) 21 July
UTC 21:20
UTC 21:40
Altitude (km)
WVD (g/m3)

360

Figure 7. Distribution of water vapor density Profiles (WVD) derived from GNSS tomographic result with the temporal resolution of 20 minutes, where (a1)-(h1), (a2)-(h2) and (a3)-(h3) refer to the location of SPP, PEN and TKL rain gauge over the period of UTC 18:00-20:40, UTC 18:00-20:40 and UTC 19:00-21:40, 21 July 2015, respectively, the blue line represents the beginning epoch of precipitation.

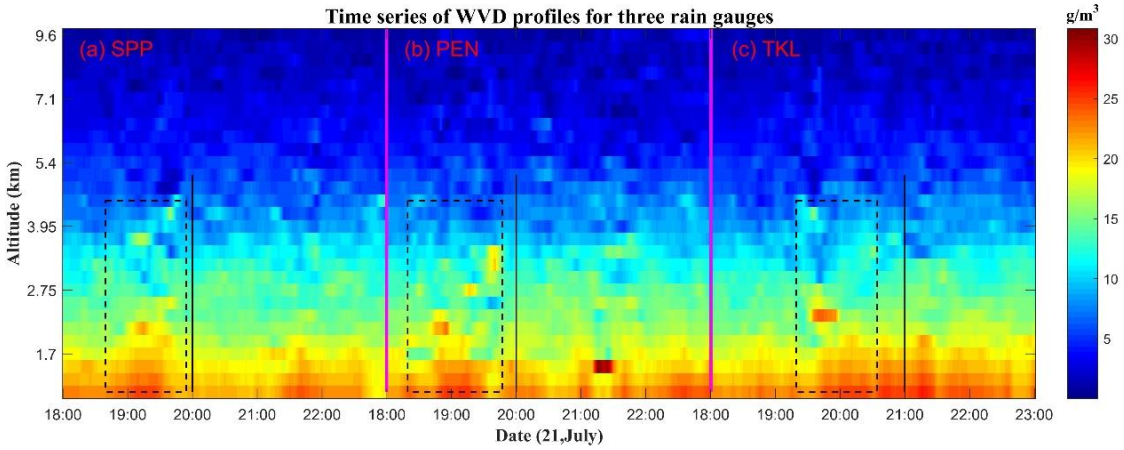

Figure 8. Time series of water vapor density (WVD) profiles derived from GNSS tomographic result with the temporal resolution of 1 minute for the locations of three rain gauges over the period of UTC 18:00 to 23:00, 21 July 2015, where the rainfall happened at UTC 20:00 21 July for (a) SPP and (b) PEN rain gauges while the rainfall occurred at UTC 21:00 21 July for (c) TKL rain gauge. The WVD profiles with drastic vertical motion are marked by the black dotted rectangles for three rain gauges while the locations of black solid lines are the starting time of rainfall

To verify the phenomenon observed above, another period (UTC 0 to 4, 23 July 2015) at PEN and TMS rain gauges is selected while the hourly rainfall information is presented in Table 2. Figures 9 and 10 both reflect that the change in water vapour profiles at PEN and TMS stations are similar to that of above conditions. The water vapour content at PEN and TMS is increased at altitudes of 2.5 km and 3.2 km, respectively, some 1-2 hours before onset of rainfall and returns to its average value at the moment that the rainfall is about to begin. One possible explanation for this is that: before onset of rainfall, the atmospheric water vapour was conditionally unstable with intense vertical movement as proved by Brenot et al., (2006). The ascending motion of water vapour in

the lower atmosphere and the descending motion of water vapour in the upper atmosphere significantly increases the water vapour content at a certain height where hydrometeors are formed. The hydrometeors consist of liquid water and icy hydrometeors, formation of which is random in time and space. Due to the delays to satellite signals induced by liquid water and icy species generally being much smaller than the water vapour species-induced delays, therefore, these delays cannot be reflected evidently in the case of GNSS observations. These newly-generated hydrometeors particles form raindrops with a continual accretion thereof. When the atmosphere is unable to support the weight of the formed raindrop, the drop falls as rain. The formation of hydrometeors particles and raindrops require some time, hence the intense vertical movement of atmospheric water vapour before onset of rainfall. The time taken to generate hydrometeors and raindrops provides the possibility of now-casting rainfall based on the GNSS technique.

Table 2. Hourly Rainfall for the selected four rain gauges over the period UTC 1 to 5, 23 July 2015 (Unit: mm)

Station / Date	PEN	TMS
0, 23 July	0	0
1, 23 July	0	0
2, 23 July	4.5	16.5
3, 23 July	0.5	4.5
4, 23 July	0	0.5

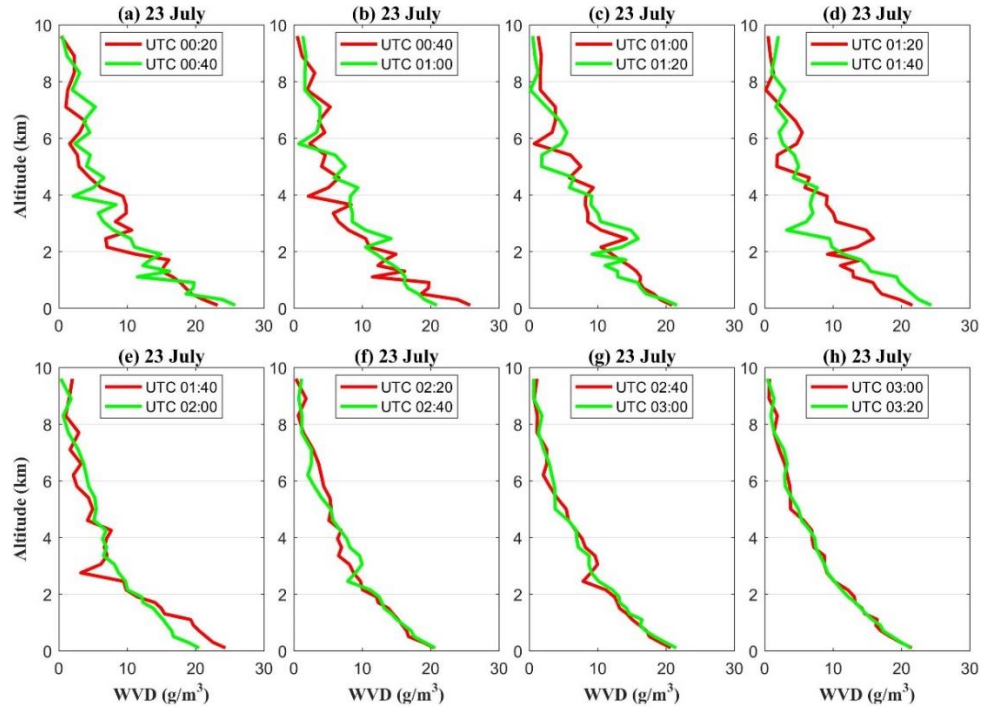

399

400 Figure 9. Distribution of water vapor density (WVD) profiles from GNSS tomographic result with

401 the temporal resolution of 20 minutes for the location of PEN rain gauge over the period of UTC

402 00:20 to 03:20, 23 July 2015

403

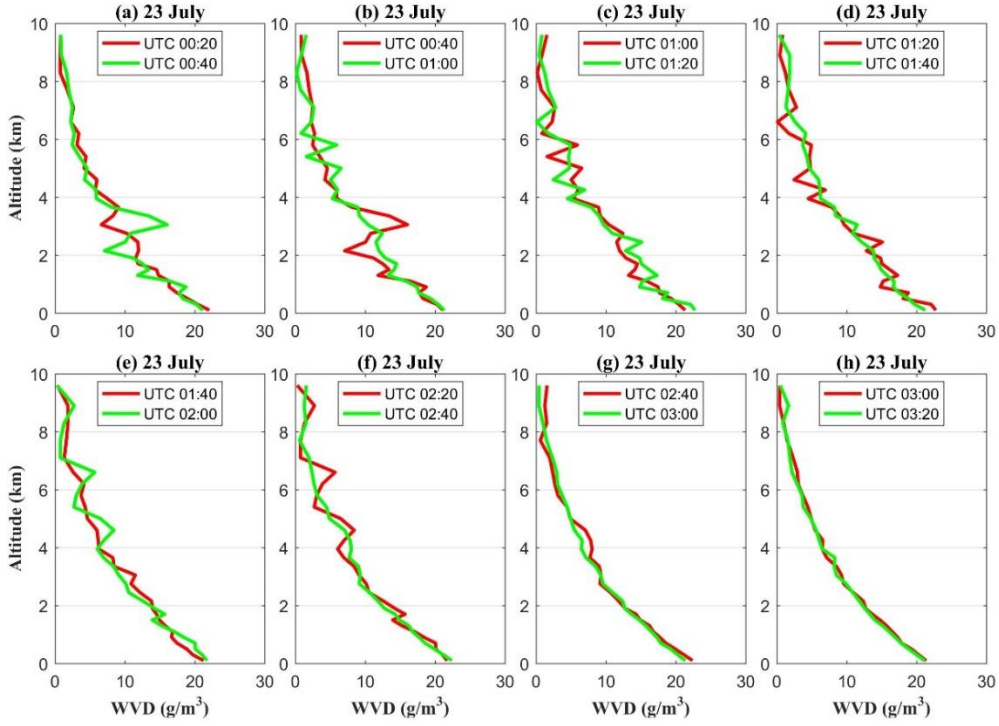

404

405 Figure 10. Distribution of water vapor density (WVD) profiles from GNSS tomographic result

406 with the temporal resolution of 20 minutes for the location of TMS rain gauge over the period of

UTC 00:20 to 03:20, 23 July 2015

The 4-d distribution of atmospheric water vapour for the period UTC 18:00 to 20:20, 21 July 2015 is presented with a spatio-temporal resolution of 20 minutes and 20 layers to an altitude of 5 km, respectively (Figure 11). According to the hourly rainfall recordings at 45 rain gauges in this area, most parts of the experimental area suffered heavy rainfall at UTC 20:00, 21 July 2015 that lasted for several hours. It can be found from Figure 11 that the significant vertical motion of water vapour observed over the period from UTC 18:00 to 19:40, and returns to its relatively stable condition at UTC 20:00 but with a lower water vapour content in most layers. The main reason for this may be water vapour transfer to the liquid water particles and icy hydrometeors, which have little impact on the delay of satellite signals and cannot be reflected evidently by the GNSS technique. For the period of heavy rainfall that occurred after UTC 20:00, the atmospheric water vapour profiles were relatively stable with slight vertical variation in water vapour content. In addition, it can be concluded that the place at which hydrometeors were generated in the lower atmosphere is possibly where rainfall occurred. Therefore, where heavy rainfall occurred is possibly predictable before the onset of rainfall according to the 4-d atmospheric water vapour variations at different altitudes derived from GNSS tomography. It also can be found that there is the horizontal motion of atmospheric water vapor as well in different layers, especially at the bottom layers. This is because the happening of rainfall requires the enough water vapor supplement, the horizontal motion of water vapor at the bottom layers implies the continuous water vapor transportation.

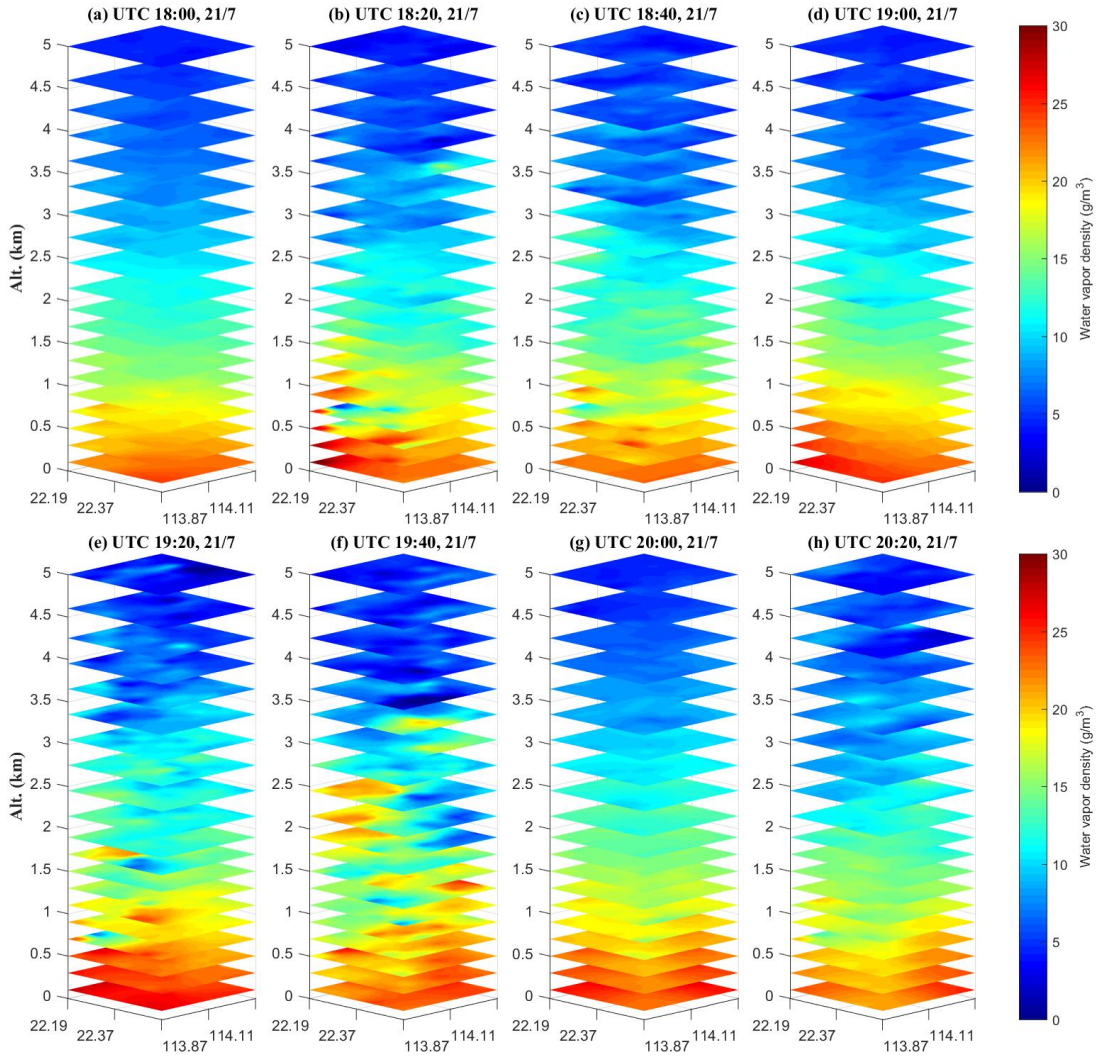

Figure 11. Three-dimensional distribution of atmospheric water vapor density derived from GNSS tomographic result with the temporal resolution of 20 minutes over the period of UTC 18:00 to 20:20, 21 July 2015 with 20 layers from the ground to 5km

5 Conclusion

GNSS sensing water vapour is an effective, practical technique, which able to reflect 2-d and 4-d atmospheric water vapour variations during the formation and lifecycle of heavy rainfall. 2-d PWV time series data derived from GNSS observations are first compared with hourly rainfall measurements, which reveals the continuous increasing trend in PWV before the onset of rainfall and returns to its average value after rainfall. In addition, it is also found that the variations of surface temperature and relative humidity have day-periodicity and are mainly caused by the variations in solar radiation during no rain periods, but their changes are disturbed by rainfall

during rainfall periods.

A 4-d water vapour reconstruction technique is performed using GNSS data to analyse the vertical water vapour movement during rainfall period. It is found that significant vertical motion occurred about 1-2 hours before the arrival of rainfall and this was reflected by the ascending and descending motions of water vapour in the lower and upper atmosphere, respectively. Hydrometeors are then formed at a certain altitude where sufficient water vapour was concentrated. The formation of hydrometeors and raindrops requires some time, which makes it possible for the forecasting of now-casting rainfall. At the moment of onset of rainfall, the water vapour profiles return to their average values at different altitudes and show a relative stable condition but with a decreasing trend in the water vapour content in the lower atmosphere. In addition, the place where the rainfall is most possible happened may be forecasted by locating out the location of the point of decreasing water vapour content in the lower atmosphere. These results revealed that rainfall had a direct relationship with atmospheric water vapour content as well as the vertical variations of water vapour density profiles, which further manifested the significant potential of the GNSS technique for monitoring and forecasting during the lifecycle of rainfall event.

Acknowledgement: The authors would like to thank IGAR for providing access to the web-based IGAR data. The Lands Department of HKSAR is also acknowledge for providing GNSS and meteorological data from the Hong Kong Satellite Positioning Reference Station Network (SatRef) and the corresponding rainfall data. This research was supported by the Key projects of National Natural Science Foundation (41730109).

References:

Akilan A.; Azeez K K A.; Balaji S, et al. GPS derived Zenith Total Delay (ZTD) observed at tropical locations in South India during atmospheric storms and depressions. *Journal of Atmospheric and Solar-Terrestrial Physics*. 2015, 125, 1-7.

Alshawaf, F. Constructing water vapor maps by fusing InSAR, GNSS and WRF data. Karlsruhe, Karlsruher Institut für Technologie (KIT), Dissertation. 2013.

Askne J.; Nordius H. Estimation of tropospheric delay for microwaves from surface weather data[J]. *Radio Science*. 1987, 22(03), 379-386.

Bai, Z. “Near-real-time GPS sensing of atmospheric water vapour,” Ph.D. dissertation, Queensland Univ. of

Technol., Brisbane, Queensland, 2004

Barindelli, S.; Realini, E., Venuti, G.; Fermi, A & Gatti, A. Detection of water vapor time variations associated with heavy rain in northern Italy by geodetic and low-cost GNSS receivers. *Earth Planets & Space*, 2018, 70(1), 28.

Bender M.; Raabe A. Preconditions to ground based GPS water vapour tomography. *Annales geophysicae*. 2007, 25(8), 1727-1734.

Bender M.; Stosius R.; Zus F.; et al. GNSS water vapour tomography–Expected improvements by combining GPS, GLONASS and Galileo observations. *Advances in Space Research*. 2011, 47(5), 886-897.

Bender M.; Dick G.; Ge M.; et al. Development of a GNSS water vapour tomography system using algebraic reconstruction techniques. *Advances in Space Research*, 2011, 47(10), 1704-1720.

Benevides P.; Catalao J.; Miranda P M A. On the inclusion of GPS precipitable water vapour in the nowcasting of rainfall. *Natural Hazards and Earth System Sciences*. 2015b, 15(12), 2605-2616.

Benevides P.; Nico G.; Catalao J.; et al. Merging SAR interferometry and GPS tomography for high-resolution mapping of 3D tropospheric water vapour. *Geoscience and Remote Sensing Symposium (IGARSS), 2015 IEEE International*. IEEE, 2015a, 3607-3610.

Bennitt G V.; Jupp A. Operational assimilation of GPS zenith total delay observations into the Met Office numerical weather prediction models. *Monthly Weather Review*, 2012, 140(8), 2706-2719.

Bevis M.; Businger S.; Herring T A.; et al. GPS meteorology: Remote sensing of atmospheric water vapor using the Global Positioning System. *Journal of Geophysical Research: Atmospheres*. 1992, 97(D14), 15787-15801.

Bevis M.; Businger S.; Chiswell S.; et al. GPS meteorology: Mapping zenith wet delays onto precipitable water[J]. *Journal of applied meteorology*, 1994, 33(3), 379-386.

Bi Y.; Mao J.; Li C. Preliminary results of 4-D water vapor tomography in the troposphere using GPS. *Advances in atmospheric sciences*, 2006, 23(4), 551-560.

Bock, O., Willis, P., WaDng, J., Mears, C. A high-quality, homogenized, global, long-term (1993–2008) DORIS precipitable water data set for climate monitoring and model verification, Journal of Geophysical Research, 119, 7209–7230, doi:10.1002/2013JD021124, 2014

Böhm, J., Niell, A., Tregoning, P., & Schuh, H. (2006). Global Mapping Function (GMF): A new empirical mapping function based on numerical weather model data. Geophysical Research Letters, 33(7).

Braun, John Joseph. Remote sensing of atmospheric water vapor with the global positioning system. Geophysical Research Letters, 2004, 20(23), 2631-2634.

Braun J.; Rocken C.; Liljegren J. Comparisons of line-of-sight water vapor observations using the global positioning system and a pointing microwave radiometer. *Journal of Atmospheric and Oceanic Technology*, 2003, 20(5), 606-612.

Brenot H.; Neméghaire J.; Delobbe L.; et al. Preliminary signs of the initiation of deep convection by GNSS. *Atmospheric Chemistry and Physics*, 2013, 13(11), 5425-5449.

Brenot, H., Ducrocq, V., Walpersdorf, A., Champollion, C., & Caumont, O. (2006). GPS zenith delay sensitivity evaluated from high‐resolution numerical weather prediction simulations of the 8–9 September 2002 flash flood over southeastern France. *Journal of Geophysical Research: Atmospheres*, 111(D15).

Chen B, Liu Z. Voxel-optimized regional water vapor tomography and comparison with radiosonde and numerical weather model. *Journal of geodesy*, 2014, 88(7), 691-703.

Dach, R., Lutz, S., Walser, P., Fridez, P., 2015. Bernese GNSS Software Version 5.2. Astronomical Institute, University of Bern, 884.

Flores A.; Ruffini G.; Rius A. 4D tropospheric tomography using GPS slant wet delays//Annales Geophysicae. *Springer-Verlag*, 2000, 18(2), 223-234.

Gradinarsky, L. P., Johansson, J., Bouma, H. R., Scherneck, H. G., Elgered, G.Climate monitoring using GPS,

518 Physics and Chemistry of the Earth, 27, 335–340, doi:10.1016/S1474-7065(02)00009-8, 2002.
519 Guerova G.; Jones J.; Dousa J.; et al. Review of the state of the art and future prospects of the ground-based GNSS
520 meteorology in Europe. *Atmospheric Measurement Techniques*, 2016, 9(11), 1-34.
521 Heublein M.; Zhu X X.; Alshawaf F.; et al. Compressive sensing for neutrospheric water vapor tomography using
522 GNSS and InSAR Observations[C]//Geoscience and Remote Sensing Symposium (IGARSS), *2015 IEEE*
523 *International*. IEEE, 2015, 5268-5271.
524 Herring, T.A., King, R.W., McClusky, S.C., 2010. Documentation of the GAMIT GPS Analysis Software Release
525 10.4. Department of Earth and Planetary Sciences, Massachusetts Institute of Technology, Cambridge,
526 Massachusetts.
527 Hirahara K. Local GPS tropospheric tomography. *Earth, planets and space*, 2000, 52(11), 935-939.
528 JMA (2013) Outline of the operational numerical weather prediction at the Japan Meteorological Agency.
529 Appendix to WMO technical progress report on the global data-processing and forecasting system (GDPFS) and
530 numerical weather prediction (NWP) research.
531 http://www.jma.go.jp/jma/jma-eng/jma-center/nwp/outline2013-nwp/index.htm. Accessed 30 Aug 2017
532 Kacmarík, M., Douša, J., Dick, G., Zus, F., Brenot, H., Möller, G., Pottiaux, E., Kapłon, J., Hordyniec, P.,
533 Václavovic, P., Morel, L. Inter-technique validation of tropospheric slant total delays, Atmospheric Measurement
534 Techniques, 10, 2183-2208, doi:10.5194/amt-10-2183-2017, 2017
535 Liu J.; Yao Y.; Sang J. A new weighted mean temperature model in China. *Advances in Space Research*, 2018,
536 61(1), 402-412.
537 Liu Z.; Wong M S.; Nichol J.; et al. A multi-sensor study of water vapour from radiosonde, MODIS and
538 AERONET: a case study of Hong Kong. *International Journal of Climatology*, 2013, 33(1), 109-120.
539 Ning, T. a Elgered, G. Trends in the atmospheric water vapour content from ground-based GPS: the impact of the
540 elevation cutoff angle, IEEE Journal of Selected Topics in Applied Earth Observations and Remote Sensing, 5,
541 744–751, doi:10.1109/JSTARS.2012.2191392, 2012.
542 Perler D.; Geiger A.; Hurter F. 4D GPS water vapor tomography: new parameterized approaches. Journal of
543 Geodesy, 2011, 85(8), 539-550.
544 Rius A.; Ruffini G.; and Cucurull L.; "Improving the vertical resolution of ionospheric tomography with GPS
545 occultations," *Geophys*. Res. Lett. 1997, 24(18), 291–2294.
546 Rohm, W.: The ground GNSS tomography – unconstrained approach, Advances in Space Research, 51, 501–513,
547 doi:10.1016/j.asr.2012.09.021, 2013
548 Rohm W, Bosy J. Local tomography troposphere model over mountains area. *Atmospheric Research*, 2009, 93(4),
549 777-783.
550 Rohm W.; Bosy J. The verification of GNSS tropospheric tomography model in a mountainous area . *Advances in*
551 *Space Research*, 2011, 47(10), 1721-1730.
552 Saastamoinen, J. Atmospheric correction for the troposphere and stratosphere in radio ranging satellites. *The use of*
553 *artificial satellites for geodesy*, 1972, 247-251.
554 Saito K.; Shoji Y.; Origuchi S.; et al. GPS PWV Assimilation with the JMA Nonhydrostatic 4DVAR and Cloud
555 Resolving Ensemble Forecast for the 2008 August Tokyo Metropolitan Area Local Heavy Rainfalls//*Data*
556 *Assimilation for Atmospheric, Oceanic and Hydrologic Applications (Vol. III)*. Springer, Cham, 2017, 383-404.
557 Shoji, Y. (2009). Assimilation of nationwide and global gps pwv data for a heavy rain event on 28 july 2008 in
558 hokuriku and kinki, japan. SOLA - Scientific Online Letters on the Atmosphere, 5(1), 45-48.
559 Shoji, Y. (2013). Retrieval of water vapor inhomogeneity using the japanese nationwide gps array and its potential
560 for prediction of convective precipitation. Journal of the Meteorological Society of Japan, 91(1), 43-62.
561 Shangguan, M., Bender, M., Ramatschi, M., Dick, G., Wickert, J., Raabe, A., Galas, R.
562 GPS tomography: validation of reconstructed 3-D humidity fields with radiosonde profiles, Annales Geophysicae,

31, 1491-1505, doi:10.5194/angeo-31-1491-2013, 2013.

Skone S.; Hoyle V. Troposphere Modeling in a Regional GPS Network. *Positioning*, 2005, 4(1&2), 230-239.

Troller M.; Geiger A.; Brockmann E.; et al. Determination of the spatial and temporal variation of tropospheric water vapour using CGPS networks. *Geophysical Journal Internationa*l, 2006, 167(2), 509-520.

Vey, S., Dietrich, R., Rülke, A., Fritsche, M., Steigenberger, P., Rothacher, M.: Validation of precipitable water vapour within the NCEP/DOE reanalysis using global GPS observations from one decade, Journal of. Climate, 23, 1675–1695, doi:10.1175/2009JCLI2787.1, 2010.

Wang, X., Wang, X., Dai, Z., et al. Tropospheric wet refractivity tomography based on the BeiDou satellite system. *Advances in Atmospheric Sciences*, 2014, 31(2), 355-362.

Wu, D., Zhao, X., Liang, S., Zhou, T., Huang, K., Tang, B., and Zhao W. (2015). Time-lag effects of global vegetation responses to climate change. Global Change Biology, 21(9), 3520-3531.

Yao Y B.; Zhu S.; Yue S Q. A globally applicable, season-specific model for estimating the weighted mean temperature of the atmosphere. *Journal of Geodesy*, 2012, 86(12), 1125-1135.

Yao Y B.; Zhao Q Z.; Zhang B. A method to improve the utilization of GNSS observation for water vapor tomography. *Annales Geophysicae (09927689)*, 2016, 34(1), 143-152.

Yao Y.; Zhao Q. Maximally Using GPS Observation for Water Vapor Tomography. *IEEE Transactions on Geoscience and Remote Sensing*, 2016, 54(12), 7185-7196.

Yao Y.; Zhao Q. A novel, optimized approach of voxel division for water vapor tomography[J]. *Meteorology and Atmospheric Physics*, 2017, 129(1), 57-70.

Yao Y.; Shan L.; Zhao Q. Establishing a method of short-term rainfall forecasting based on GNSS-derived PWV and its application. *Scientific reports*, 2017, 7(1), 12465.

Yao Y.; Zhang B.; Xu C. and Yan, F. Improved one/multi-parameter models that consider seasonal and geographic variations for estimating weighted mean temperature in ground-based GPS meteorology. *Journal of Geodesy*, 2014, 88(3), 273-282.

Yao Y B.; Liu J H.; Zhang B.; et al. Nonlinear relationships between the surface temperature and the weighted mean temperature. *Geomatics & Information Science of Wuhan University*, 2015, 40(1), 112-116.

Zhang K.; Manning T.; Wu S.; et al. Capturing the signature of severe weather events in Australia using GPS measurements. *IEEE Journal of Selected Topics in Applied Earth Observations and Remote Sensing*, 2015, 8(4), 1839-1847.

Zhao Q.; Yao Y. An improved troposphere tomographic approach considering the signals coming from the side face of the tomographic area//Annales Geophysicae. *Copernicus GmbH*, 2017b, 35(1), 87-95.

Zhao Q.; Yao Y.; Cao X.; et al. Accuracy and reliability of tropospheric wet refractivity tomography with GPS, BDS, and GLONASS observations. *Advances in Space Research*, 2018c. DOI:10.1016/j.asr.2018.01.021

Zhao Q.; Yao Y.; Yao W. A troposphere tomography method considering the weighting of input information[C]//Annales Geophysicae. *Copernicus GmbH*, 2017a, 35(6), 1327-1340.

Zhao Q.; Yao Y.; Yao W. GPS-based PWV for precipitation forecasting and its application to a typhoon event. *Journal of Atmospheric and Solar-Terrestrial Physics*, 2018a, 167, 124-133.

Zhao Q., Yao Y., Cao X., Zhou F. and Xia P. An Optimal Tropospheric Tomography Method Based on the Multi-GNSS Observations. *Remote Sensing*, 2018d, 10(2), 234.

Zhao Q.; Yao Y.; Yao W.; et al. Real-time precise point positioning-based zenith tropospheric delay for precipitation forecasting. *Scientific reports*, 2018b, 8(1), 7939-7939.

Zhao, Q., Yao, Y., Yao, W. Q., & Li, Z. Near-global GPS-derived PWV and its analysis in the El Niño event of 2014–2016. Journal of Atmospheric and Solar-Terrestrial Physics, 2018e, 179, 69-80.